



Steam reforming of acetone over Ni- and Co-based catalysts: Effect of the composition of reactants and catalysts on reaction pathways

Adriano H. Braga^a, Elaine R. Sodré^b, João Batista O. Santos^a, Clelia M. de Paula Marques^b, José Maria C. Bueno^{a,*}

^a Department of Chemical Engineering, Federal University of São Carlos (UFSCar), P.O. Box 676, 13565-905 São Carlos, São Paulo, Brazil

^b Department of Chemistry, Federal University of São Carlos (UFSCar), P.O. Box 676, 13565-905 São Carlos, São Paulo, Brazil

ARTICLE INFO

Article history:

Received 16 December 2015
Received in revised form 5 March 2016
Accepted 23 April 2016
Available online 25 April 2016

Keywords:

Acetone reforming
Hydrogen production
Reaction mechanism
Ni catalyst
Co catalyst
Heterogeneous catalysis
Biomass conversion

ABSTRACT

The properties of Ni/Co/Co-Ni/MgAl₂O₄ catalysts in the steam reforming of acetone (SRA) were investigated regarding the metallic composition and nature of catalytic site. The catalysts were characterized by nitrogen physisorption, X-ray diffraction, X-ray absorption spectroscopy, transmission electron microscopy, and temperature programmed reduction and desorption of acetone. Experimental data revealed that the acetone conversion pathway on the Co, Co-Ni, or Ni catalysts was strongly dependent on the nature of the metal, reaction temperature, and the oxidation state of the metal atoms in nanoparticles surface atoms. Reaction data indicated that the acetone decomposition on reduced metal catalysts at high temperatures (>350 °C) occurred mainly via the H—C and C—CO bonds cleavage, leading to the formation of CO, H₂, and C on the metal surface. At low temperatures (200 °C) and in the presence of H₂ in the reactor feed, the Ni catalyst catalyzed the hydrogenation of the CO and CH_x species formed from acetone activation on the metallic sites, producing CH₄. For Co-containing catalysts, at low temperatures (200–350 °C) the metal nanoparticles surface was in a higher oxidation degree and promoted the oxidation of acetone. At high temperatures (>350 °C), the hydrogenation of CH_x and CO species to CH₄ was determined by the nanoparticle oxidation degree, which decreased in the order Ni > Co-Ni > Co. With increased temperature, the CH_x species decomposed to C and H₂, instead of being hydrogenated to CH₄. The oxidation of C by H₂O was favored on Co-containing catalysts. The reaction pathways are discussed based on theoretical data obtained from the literature.

© 2016 Elsevier B.V. All rights reserved.

1. Introduction

The need to reduce greenhouse gases emissions, combined with an increasing demand for energy, has generated substantial interest in developing of alternative routes for energy production, especially from renewable feedstocks [1]. Hydrogen is important for the production of clean fuels by hydroprocessing. It is an effective alternative to fossil fuels and can be used in highly efficient systems such as fuel cells to produce energy in an environmentally friendly fashion [2]. Hydrogen can be produced from the biomass-derivatives gasification process by steam reforming.

The pyrolysis of biomass produces a liquid “bio-oil” composed of oxygenated compounds and H₂O. The main light molecules are aldehydes, alcohols, carboxylic acid, cresols, and ketones, here collectively denoted C_xH_yO_z, as well as carbohydrates and lignin [3]. The light fraction, can be directly steam reformed to produce H₂,

which has received special attention due to the associated environmental benefits [4,5]. In the steam reforming process, the catalyst assists the cleavage of C—H, C—C, and O—H bonds, with the fragments recombining to produce CO, CO₂, and H₂. Noble metals such as Rh and Ir are promising catalysts due to their greater ability in breaking C—C bonds. However, the high cost of noble metals has shifted attention to Ni and Co catalysts, which are also effective in breaking C—C bonds and highly active in steam reforming [6–10]. Ni-based catalysts have been used in steam reforming of model bio-oil molecules such as acetone and acetic acid.

A series of studies have investigated the influence of independent variables including the reaction temperature, space velocity, and steam-to-carbon molar ratio (S/C) in the H₂ yields and carbon deposition [5,11–30]. The performance of a catalyst is intrinsically dependent on the nature of the active metal, the metal particle size, the support, and the promoters [7,8,25,31–37].

Due the complexity of bio-oil, model molecules have been studied in steam reforming reactions [18,38]. Ethanol, as an example of a biomass derived light molecule, has been extensively studied in steam reforming [6]. Reforming of bio-oil light frac-

* Corresponding author.

E-mail address: jmc@ufscar.br (J.M.C. Bueno).

tion compounds involves the cleavage of C–H and C–C bonds, which, compared to methane, are easier to activate and require lower temperatures. The pathway for reforming these compounds, as proposed for ethanol, is different from the one extensively described for CH₄ steam reforming [39]. Previous studies of reforming of ethanol have revealed that the pathway depends on the nature of the metal [6,40]. On Ni/Al₂O₃ catalysts at low temperatures (<650 K), the decomposition of ethanol occurs via the acetaldehyde intermediate, which decomposes to species such as –CH_x and –CO, leading to the formation of equimolar mixtures of CH₄ and CO [39]. At high temperatures, the steam reforming of ethanol occurs via oxidation of –CO and decomposition of –CH_x to C and H₂. The pathway for this reaction on Co/SiO₂ is apparently different to that on Ni-based catalysts, where the adsorbed CH_x species formed by the cleavage of C–C bonds at low temperature are strongly adsorbed, hindering the hydrogenation to CH₄ [40].

The mechanism for steam reforming of acetone, another bio-oil component, was proposed using DFT calculations for Co [41] catalysts. Different from the mechanism proposed for ethanol [42], C–H scission is favored relative to C–C; therefore, the decomposition to C and H₂ might restrict the formation of CH₄ via hydrogenation of –CH_x species. Although Co-based catalysts are able to activate H₂O for reforming of C_xH_yO_z compounds, producing H₂ [43,44], Co adsorbs O and OH more strongly than Ni. Adsorbed O and OH species on Co have negative free energies [45], indicating greater coverage of these species on Co than on Ni. Thermodynamic analysis of the oxidation and re-reduction of cobalt nanoparticles shows that they are likely to be oxidized in the presence of an H₂O–H₂ mixture [46]. This indicates a high susceptibility to oxidation for Co, opposed to Ni, which is favored with decreasing particle size [46].

In this work, the influence of the nature of the metal on catalytic properties and the reaction pathway for steam reforming of acetone was evaluated using temperature-resolved characterization of the reaction and the oxidation state of the metal particles in Ni-, Co-Ni-, and Co-based catalysts. Using experimental measurements and theoretical data from the literature, evaluation of the dependence of the pathway for steam reforming of acetone on the oxi-reduction properties of the metal and their influence on selectivity and carbon accumulation with time on stream is made.

2. Methodology

2.1. Catalyst preparation

The catalysts were prepared by incipient wetness impregnation of Ni(NO₃)₂·6H₂O and Co(NO₃)₂·6H₂O onto a MgAl₂O₄ support synthesized by the sol-gel method, as previously described by Avila-Neto et al. [47]. The appropriate amounts of the Ni and Co salts were dissolved in ethanol in order to give total metal loadings of 8 wt.%. In the case of the bimetallic sample, the Co and Ni salts were diluted in ethanol to obtain a sample with 4 wt.% of Co and 4 wt.% of Ni. The solution was then added to the support and the final material was dried overnight under vacuum. Afterwards, the samples were calcined at 550 °C, with heating from room temperature at 3 °C min⁻¹, and kept at 550 °C for 6 h under a flow of synthetic air. The catalysts were labeled as Ni, Co-Ni, and Co, representing Ni/MgAl₂O₄, Co-Ni/MgAl₂O₄, and Co/MgAl₂O₄, respectively.

2.2. Characterization

XRD patterns were obtained with a Rigaku Multiflex instrument, in the 2θ range from 10 to 90°, with pass of 0.1°. The peaks were identified by comparison with the diffraction patterns of cubic

MgAl₂O₄, cubic Co₃O₄, fcc NiO, and cubic NiCo₂O₄ obtained from the ICSD database.

The surface areas of the calcined catalysts were determined by N₂ adsorption, based on the BET equation, using a Quantachrome Autosorb 1C instrument.

Temperature programmed reduction (TPR) was performed with a Micromeritics AutoChem II 2920 system. 150 mg of catalyst and support were placed in a quartz U reactor and reduced by heating from room temperature up to 1000 °C under a 30 mL min⁻¹ flow of a 10% H₂/N₂ mixture. The H₂ consumption was measured with a previously calibrated thermal conductivity detector.

Temperature programmed desorption of acetone was performed using the same TPR system. The catalysts (150 mg) were reduced at 750 °C for 1 h under a 30 mL min⁻¹ flow of a 10% H₂/N₂ mixture, and were then cooled to 50 °C under a flow of He. Acetone adsorption was performed at this temperature: 4.1 μmol of gas phase acetone was introduced to the catalyst by means of a calibrated loop (1 mL), using a 30 mL min⁻¹ flow of He. The catalysts were then flushed with He for 30 min, after which the temperature was ramped from 50 to 900 °C at a rate of 10 °C min⁻¹. The products of acetone decomposition were analyzed with a Pfeiffer PrismaPlus mass spectrometer. The following mass/charge ratios and the corresponding fragments were determined: 2 (H₂); 4 (He); 28 (CO + CO₂); 15 and 16 (CH₄); 18 (H₂O); 41 (propylene); 43 and 58 (acetone); 44 (CO₂). Other *m/z* values assigned to possible products of the decomposition and condensation of acetone, such as those related to 2-propanol, mesityl oxide, acetic acid, and ethanol, were found to be negligible.

In situ FTIR spectra of adsorbed acetone were recorded during adsorption of acetone on the reduced Ni catalyst and support. The spectra were acquired in diffuse reflectance mode, employing a Harrick cell with ZnSe windows. A Thermo Scientific IS50 FT-IR spectrometer and mercury cadmium telluride (MCT) detector were used to collect the IR spectra, with resolution was of 4 cm⁻¹ and averaging 64 scans, which took around 1 min. Background spectra were acquired for the sample under He flow at each TPD temperature, before the adsorption of acetone.

The catalyst was reduced at 750 °C for 1 h under a 30 mL min⁻¹ flow of H₂. Afterwards, the sample was cooled to 50 °C under He flow, and gas phase acetone was admitted to the cell by means of a six-port switching valve and a 1.0 mL loop. The adsorption was performed using two procedures as follows: (1) one pulse of acetone (8.4 kPa, 4.1 μmol) was admitted to the sample, and a subsequent pulse of H₂ was performed; after 15 min under He, a new pulse of acetone was admitted, followed by another pulse of H₂, with recording of the FTIR spectrum between the pulses; (2) the sample was treated using three pulses of gas phase acetone (30.7 kPa, 0.15 μmol), until surface saturation, with purging with He for 15 min between the pulses.

Transmission electron microscopy (TEM) was used to determine the particle size and structure of the nanoparticles. The catalysts were reduced under H₂ (750 °C, 1 h, 10 °C min⁻¹), passivated, and then dispersed in methanol (with sonication) and dripped onto a Cu grid with a holey carbon support film. TEM images were obtained using a JEOL 2100F microscope, using a field emission gun operated at 200 kV in transmission mode with a Gatan CCD detector, and in scanning transmission mode (STEM) with a high-angle annular dark field (HAADF) detector. The spot size used for STEM was 1 nm. EELS spectra were acquired on the bimetallic catalyst to evaluate the composition of the nanoparticles. The spectra were acquired on a Gatan Tridiem Image Filt with energy resolution about 0.87 eV. For acquisition, the camera length used was of 2 cm and dispersion of 0.3 eV pixel⁻¹.

To improve the contrast in the STEM images obtained, a 1.0 nm spot size was used in the acquisition, with a camera length of around 2 cm and acceptance angle of 82.5–220 mrad. Counting

of the nanoparticles was performed using Digital Micrograph software (Gatan), with the pixel size calibrated at the nanometric scale using a standard Au sample. The identification of the nanoparticles was performed previously by EDS and EELS, and a contrast pattern was found on the images. Hence, the nanoparticles were circled using drawing tools, and the circles were white-filled and imported in a black image with the same pixel size as the original. Afterwards, a contrast filter was applied, which selected the nanoparticles, the width was estimated, and a histogram was obtained with the number of nanoparticles and width as an indication of size. A normal distribution curve was obtained, from which the mean size and standard deviation were determined.

2.3. Catalytic tests

SRA tests were performed using a fixed bed reactor consisting of 100 mg of the previously reduced catalysts, under a 100 mL min^{-1} flow of H_2 and with heating from room temperature to 550 or 750°C at $10^\circ\text{C min}^{-1}$. The samples were kept at the maximum temperature for 1 h, after which the reactor was cooled to room temperature and the H_2 flow was replaced by the SRA reaction mixture. The experiments were performed using two reactant molar compositions: (i) $\text{H}_2\text{O}/\text{acetone}/\text{He} = 10.8/1.8/87.4$ and (ii) $\text{H}_2\text{O}/\text{acetone}/\text{H}_2/\text{He} = 10.8/1.8/67.4/20.0$. In both series of experiments, the following conditions were used: $\text{H}_2\text{O}/\text{acetone}$ molar ratio = 6; $P_{\text{acetone}} = 8.4 \text{ kPa}$; and W/F_{acetone} ratio = $70.6 \text{ g}_{\text{cat}} \text{ min g}_{\text{acetone}}^{-1}$ (W = weight of catalyst and F = acetone mass flow). The temperature of the catalytic bed was increased from room temperature to 650°C in steps of 50°C .

The reactor effluent was analyzed online by gas chromatography using an Agilent 7890A gas chromatograph. Permanent gases were analyzed using a thermal conductivity detector (TCD) and PlotQ and Molsieve 5A columns, and organic species were determined using a flame ionization detector (FID) and an HP-1 column.

2.4. Stability tests

SRA stability tests were performed using a fixed bed at constant temperatures of 500 and 600°C . The catalysts were previously reduced under a 30 mL min^{-1} flow of H_2 , with heating from room temperature to 750°C at $10^\circ\text{C min}^{-1}$. The reactant mixture with composition $\text{H}_2\text{O}/\text{acetone}/\text{He} = 10.8/1.8/87.4 \text{ vol.}\%$ ($\text{H}_2\text{O}/\text{acetone}$ molar ratio = 6 and $P_{\text{acetone}} = 8.4 \text{ kPa}$) was fed to the reactor to obtain a W/F_{acetone} ratio of $70.6 \text{ g}_{\text{cat}} \text{ min g}_{\text{acetone}}^{-1}$. The reactor was maintained at 500 or 600°C for 4 h. Analysis of the reactor outflow was performed as described above. The spent catalysts were submitted to thermogravimetric analysis and the carbon accumulated was calculated from the loss of weight.

2.5. In situ measurements

The catalyst activation procedure (reduction by H_2), steam reforming of acetone, and steam reforming with H_2 addition were accompanied using X-ray absorption near edge spectroscopy (XANES) measurements in order to study the oxidation state due to the reactions, as a function of temperature and the metallic composition of the catalysts.

The catalysts were crushed and sieved to $10 \mu\text{m}$ particle size, after which a 60 mg portion was mixed with 60 mg of BN and the mixtures were compressed to form self-supporting disks. The disks were placed in a quartz tube with kapton windows and positioned axially to the X-ray beam. Experiments were performed at the DXAS beamline of the Brazilian Synchrotron Light Laboratory (LNLS), in dispersive mode, and detection employed a CCD camera.

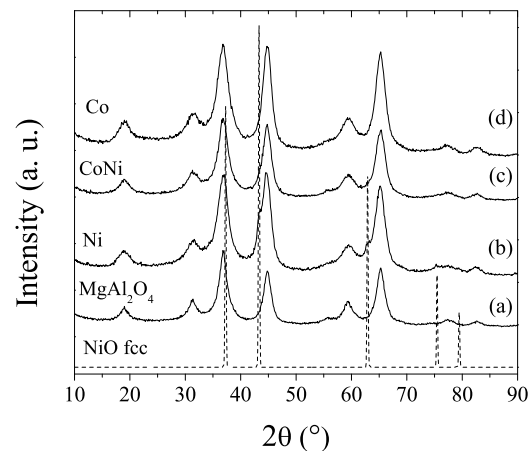


Fig. 1. XRD patterns of the synthesized MgAl_2O_4 support (a) and the supported Ni (b), Co-Ni (c), and Co (d) samples. Dashed line: XRD pattern of NiO obtained from the Inorganic Crystal Structure Database (collection code: 9866).

The samples were reduced at 750°C for 1 h, using a heating rate of $10^\circ\text{C min}^{-1}$, under a 100 mL min^{-1} flow of a 5% H_2/N_2 mixture, with data acquisition around the Co K-edge (7709 eV) and the Ni K-edge (8333 eV). The samples were then cooled to room temperature under He, followed by exposure to the streams of acetone/water. Each temperature-resolved spectrum took around 2 s to acquire. The oxi-reduction profile was obtained by linear combination fitting between each spectrum and spectra for metallic (Ni and Co foils) and oxide (Co_3O_4 , CoO , and NiO) references, in the range from -20 to 30 eV around the absorption edge. The resulting curves were the electronic state fraction as a function of temperature. Spectral calibration, normalization, and linear combination fitting were performed using Demeter software, according to the standard procedures described by Avila-Neto et al. [44].

The feed for the SRA reaction was produced by flowing He through saturators containing water and acetone, under the following conditions: molar composition $\text{H}_2\text{O}/\text{acetone}/\text{He} = 10.8/1.8/87.4$; $\text{H}_2\text{O}/\text{acetone}$ molar ratio = 6; and $P_{\text{acetone}} = 8.4 \text{ kPa}$. For the reaction with co-addition of H_2 , an H_2/He mixture was also introduced, giving a gas molar composition of $\text{H}_2\text{O}/\text{acetone}/\text{H}_2/\text{He} = 10.8/1.8/67.4/20.0$. The reactant flows were chosen to obtain $W/F = 70.6 \text{ g}_{\text{cat}} \text{ min g}_{\text{acetone}}^{-1}$. The reduction and SR reactions were accompanied by XANES and mass spectrometry (Pfeiffer Omnistar). The feeds for SR and SR with addition of H_2 were introduced to the previously reduced catalyst at room temperature, after which the temperature was ramped to 500°C , held for 30 min, and subsequently ramped to 600°C , held for 30 min, at a rate of $10^\circ\text{C min}^{-1}$.

3. Results

3.1. Textural properties and XRD analysis of the MgAl_2O_4 support and catalysts

The XRD patterns obtained for the previously calcined MgAl_2O_4 support and the supported Co, Co-Ni, and Ni samples are shown in Fig. 1. As previously reported [44,47], the diffraction peaks of the support at 31.3, 36.9, 44.9, 59.5, and 65.4° correspond to the spinel MgAl_2O_4 structure (ICSD collection code 40030). The Co and Co-Ni samples showed diffraction peaks similar to those of the support, suggesting the formation of spinel Co_3O_4 and/or NiCo_2O_4 structures with diffraction peaks overlapping those of the MgAl_2O_4 support. The Ni sample showed peaks characteristic of the support and the NiO face-centered cubic structure.

Table 1

Physical-chemical properties of the catalysts: surface area (S_{BET}), particle size (d), and reduction degree (%).

Catalyst	S_{BET} ($\text{m}^2 \text{ g}^{-1}$)	V_{pore} ($\text{cm}^3 \text{ g}^{-1}$)	D_{pore} (nm)	D_{particle} (nm) ^a	Reduction degree (%) ^b
MgAl_2O_4	156	1.9	5.4	–	–
Ni	141	1.6	4.0	18.1 (6.1)	97
Co-Ni	152	1.9	4.0	4.6 (2.5)	97/90 ^c
Co	154	1.3	3.4	4.4 (1.4)	90

^a Obtained from the TEM images of the reduced catalysts, values between parenthesis are the standard deviation.

^b Obtained by linear combination fitting from XANES measurements after reduction at 750 °C.

^c Obtained at Ni K-edge/Co K-edge.

In the textural characterization of the supports, the N_2 physisorption analyses at 77 K resulted in type IV isotherms with H3-type hysteresis loops (according to the IUPAC system) around $P/P_0 = 0.44$, as described previously by Avila-Neto et al. [44]. Table 1 shows the surface area, pore volume and size for the calcined catalysts and support. The calcined support sample (MgAl_2O_4) showed an S_{BET} value of $156 \text{ m}^2 \text{ g}^{-1}$. When the support was impregnated with 8 wt.% of the Ni, Co-Ni, and Co metal catalysts, no significant changes were observed in S_{BET} of the calcined samples compared with the S_{BET} of the support (MgAl_2O_4). These results indicate that the metal added does not obstruct the support pores.

Electron microscopy was performed in order to investigate the distribution of particle sizes. To obtain the spatial distribution between the two metals, Co and Ni, in the bimetallic catalyst it was applied electron energy loss spectroscopy (EELS), a microanalytical technique with high spatial and energy resolution. The TEM images showed particles sizes in the range of 18 nm with a broad distribution for Ni catalyst and about 4.6 and 4.4 for Ni-Co and Co catalysts respectively, after reduction with H_2 . The STEM images of the Ni, Ni-Co and Co catalysts are presented in Fig. S-1 with the respective histograms. EELS spectra obtained in some nanoparticles of the bimetallic catalyst revealed the presence of both the elements in the same particle, by the presence of the energy core-losses of $\text{Co L}_{3,2}$ and $\text{Ni L}_{3,2}$ edges (Fig. 2b and c), although in different proportions in some cases, as revealed by Fig. 2b, in which the intensity of Co core-loss is clearly higher than the intensity of Ni core-loss. These results indicated that a CoNi alloy is formed upon reduction, even though the distribution of the elements cannot be uniform, as revealed by the representative spectra showed in Fig. 2b and c.

3.2. Temperature-programmed reduction in H_2 (XANES- H_2)

The calcined Ni sample produced a XANES spectrum characteristic of NiO species [43]. The XANES profile obtained during reduction indicated that there was intense formation of Ni^0 at temperatures above 400 °C (Fig. 3). For the Co-Ni sample, the spectra at the Ni K-edge indicated the formation of Ni^0 at temperatures of about 200 °C. These results were indicative of differences in the efficiency of dissociation of H_2 on the Ni and Co-Ni samples. The reduction of NiO is controlled both by the rate of removal of lattice oxygen at the surface and by the rate of subsurface oxygen diffusion to the oxygen-depleted surface [48]. The lower temperatures for Co-Ni reduction, compared to Ni, were indicative of greater lability of O at the surface for the Co-containing sample. The spectra for the Co-containing catalysts showed features corresponding to a structure similar to $(\text{Ni},\text{Co})\text{Co}_2\text{O}_4$, where the cobalt oxide is reduced in two steps ($\text{Co}^{3+} \rightarrow \text{Co}^{2+} \rightarrow \text{Co}^0$) [49]. Higher reduction degrees of Ni or Co oxides were only achieved at temperatures of ~750 °C, which was very high compared to that expected for reduction of nanoparticles of NiO or NiCo_2O_4 . These findings, indicate an interaction between NiO and CoO with the support, which is endorsed by the TPR analyses (Supplementary material, Fig. S2). Chemical interaction of NiO with the support is likely to be favored by a smaller NiO particle size and can be attributed to the formation of species

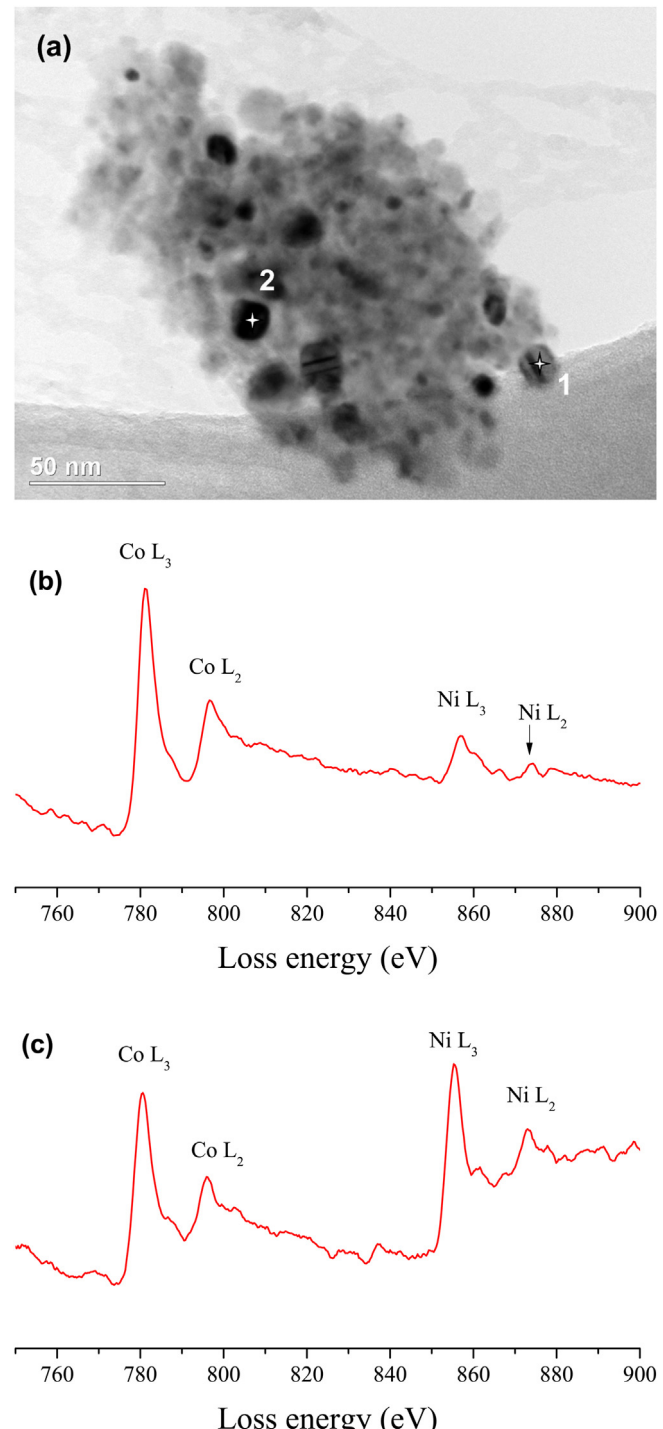


Fig. 2. TEM images of Co-Ni catalyst reduced at 750 °C (a), and respective EEL spectra showing the $\text{Co L}_{2,3}$ and $\text{Ni L}_{2,3}$ edges for highlighted point 1 in (b) and point 2 (c).

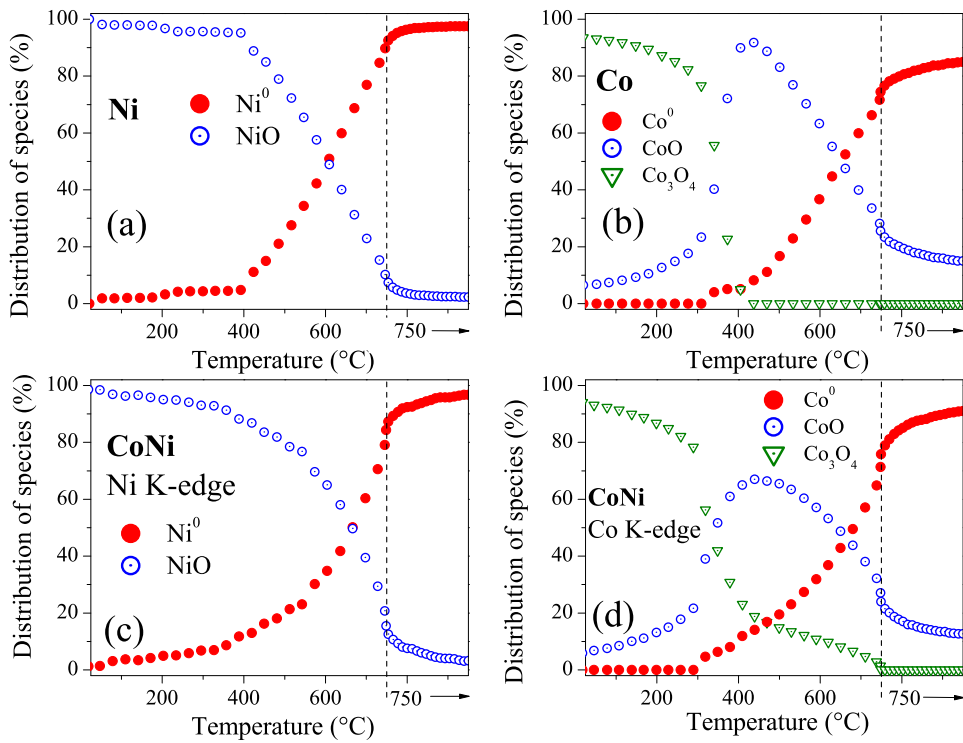
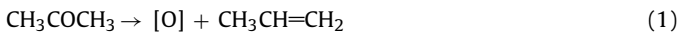


Fig. 3. Reduction profiles obtained by linear combinations of XANES spectra at the Ni and Co K-edges and reference data for the metals (Ni and Co) and oxides (NiO, CoO, and Co_3O_4), at the Ni K-edge of the Ni (a) and Co-Ni (c) samples, and at the Co K-edge of the Co (b) and Co-Ni (d) samples.

such as aluminate (Ni-O-Al) and incorporation of Al^{3+} into the NiO surface [50]. Similar behavior is expected for CoO.

3.3. Temperature-programmed desorption of acetone

Fig. 4 shows the desorption spectra of the compounds. The mass fragment with $m/z = 15$ was used to represent CH_4 , instead of $m/z = 16$, in order to avoid large contributions from fragments of CO , CO_2 , and H_2O . For other products desorbed, the most abundant fragments are provided in Table S1. The TPD profile of acetone adsorbed on the support (MgAl_2O_4) presented low-temperature peaks (maximum at ca. 250 °C) that were indicative of desorption of acetone ($m/z = 43$). The formation of propylene ($m/z = 41$) is favored with saturation coverage (Fig. S3) over oxides by acetone reduction (Eq. (1)). With increasing saturation of the surface with acetone, propylene formation catalyzed by the support surface was observed over the Ni, Co-Ni, and Co catalysts (Fig. S3).



The Ni, Co-Ni, and Co catalysts showed the formation of H_2 ($m/z = 2$) with peaks maxima at 150–200 and 300 °C. Both $\text{CO} + \text{CO}_2$ ($m/z = 28$) and CO_2 ($m/z = 44$) were desorbed at about 300 °C. The temperatures for desorption of H_2 and CH_4 were more strongly dependent on the nature of the metal. H_2 and CH_4 were desorbed at higher temperatures for the Co-containing catalyst, compared to the Ni-containing catalyst. In the low temperatures region of initial H_2 desorption, CH_4 ($m/z = 15$) was also desorbed, indicating that acetone cleavage could occur via the C–H and C–CO bonds, with formation of H_2 , H_3CO^* , and $^*\text{CH}_x$ species on the metal. The $^*\text{CH}_3$ species was hydrogenated to CH_4 in a lower temperature region than desorption of CO and intense desorption of H_2 . There was an increase in CH_4 ($m/z = 15$) at low temperature with an increase of the Ni content in the catalyst (Fig. 4), indicating that the hindrance of hydrogenation of intermediates from acetone activation was higher for Co-containing than for Ni catalysts, and that these

intermediates were decomposed to CO and H_2 at higher temperatures. CO_2 , which was probably formed by disproportionation of CO in the shift reaction, was desorbed at temperatures exceeding around 240 °C.

3.4. FTIR of adsorbed acetone

Fig. 5 shows the spectra of acetone adsorbed on the Ni catalyst under two different conditions: (i) surface saturation, and (ii) successive pulses of acetone and H_2 . The intense band at 1706 cm^{-1} was characteristic of stretching vibrations of $\text{C}=\text{O}$ of acetone in multilayer configuration [51]. The bands present at 1448 and 1374 cm^{-1} could be attributed to symmetric ($\delta_s(\text{CH}_3)$) and asymmetric ($\delta_{as}(\text{CH}_3)$) deformation of CH_3 [51]. The band at 1241 cm^{-1} could be identified as the C–C–C stretching vibration of acetone ($\nu(\text{CCC})$). These bands indicate the presence of acetone in configuration $\eta^1(\text{O})$, bonded by the to both Ni^0 or Al^{3+} Lewis acid surface. Bands at 1633 cm^{-1} ($\nu(\text{C}=\text{C}=\text{O})$) and 1607 cm^{-1} ($\nu(\text{C}=\text{C})$) suggested the presence of the enolate isomer of acetone on the Ni^0 and Al atoms. The band at 1607 cm^{-1} could also be attributed to $\nu(\text{C}=\text{C})$ of mesityl oxide.

In the C–H stretching region, bands appeared at 2973, 2929, 2874, and 3012 cm^{-1} when the saturation of the surface occurred (Fig. 5a). In the presence of H_2 , the features of the bands changed, with increasing intensity of bands at 2973 and 2874 cm^{-1} , which could be attributed to acetyl species on the metal surface [52]. Fig. S4 shows the FTIR spectra during TPD-acetone, increasing temperature the intensity decreased of bands characteristic of adsorbed acetone in $\eta^1(\text{O})$ configuration at 1706, 1448 and 1374 cm^{-1} and the intensity increased of band characteristic of adsorbed enolate-isomer at 1634 cm^{-1} . These results indicate that increasing temperature acetone adsorbed in $\eta^1(\text{O})$ is converted to enolate-isomer may be via $\eta^2(\text{C},\text{O})$ configuration.

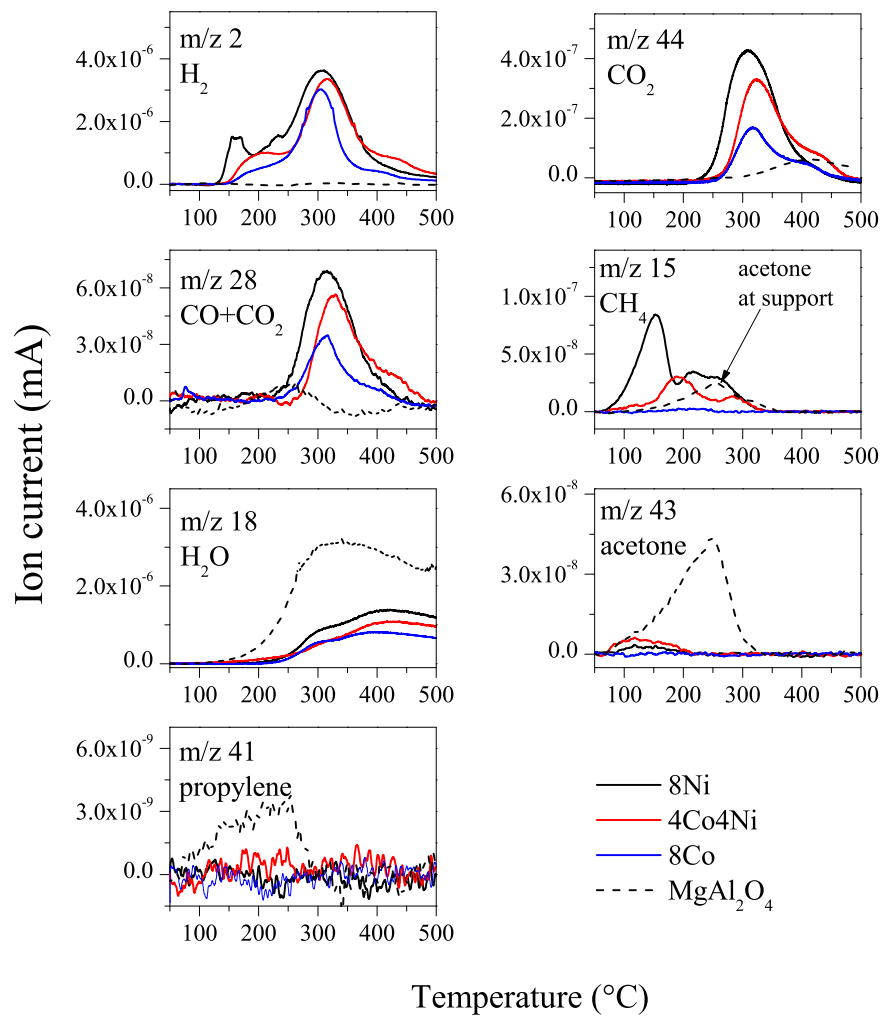


Fig. 4. TPD spectra for the decomposition products of acetone on the Co, Co-Ni, and Co catalysts, indicating the mass fragments used for each product.

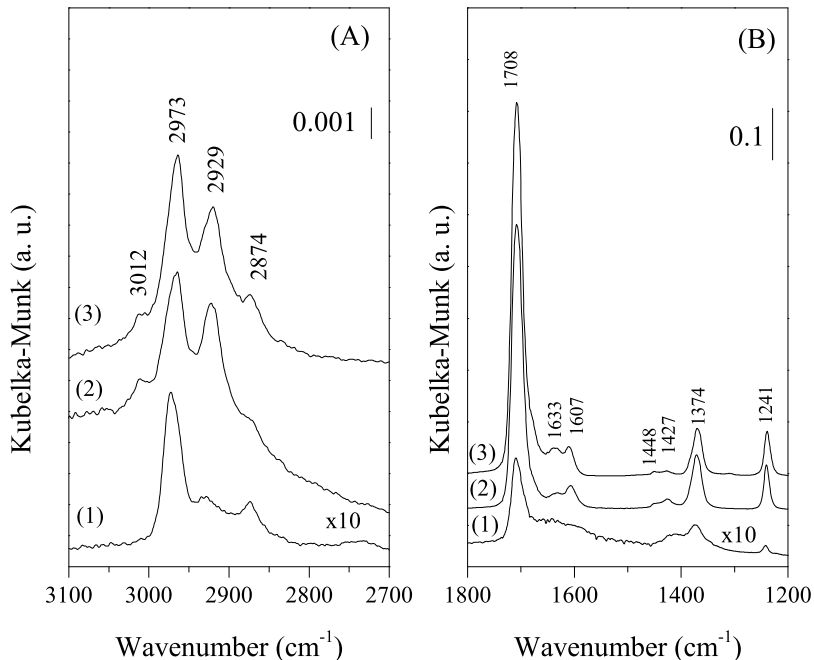


Fig. 5. FTIR spectra of Ni catalyst exposed to acetone or acetone-H₂: (1) one pulse of gas phase acetone on reduced Ni catalyst, followed by a pulse of pure H₂; (2) surface saturation with gas phase acetone on reduced Ni catalyst and (3) surface saturation of acetone on MgAl₂O₄ support.

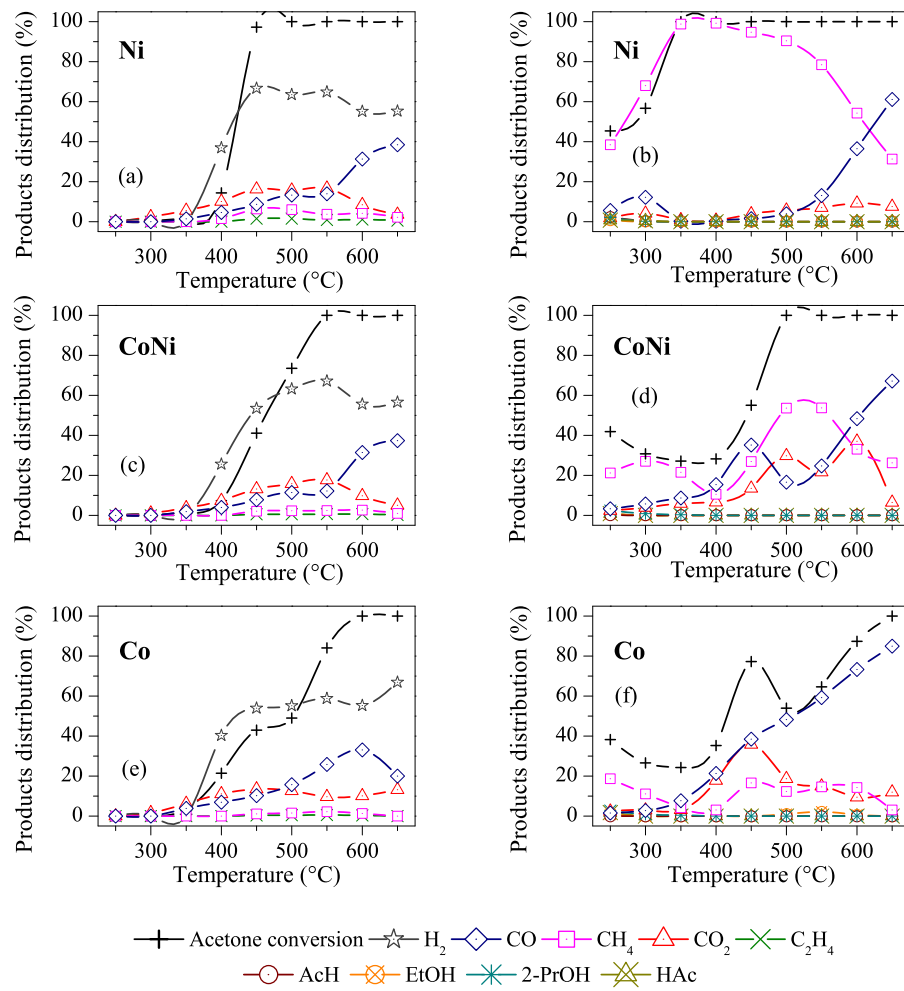


Fig. 6. Acetone conversion (+) and distribution of various chemical species produced during the SRA reaction, as a function of temperature, for a reactor with $P_{\text{acetone}} = 8.4 \text{ kPa}$, and feeds with two compositions: (a) Ni, (c) Co-Ni, and (e) Co catalysts in SRA using $\text{H}_2\text{O}/\text{acetone}/\text{He} = 10.8/1.8/87.4$; (b) Ni, (d) Co-Ni, and (f) Co catalysts in SRA with addition of H_2 , using $\text{H}_2\text{O}/\text{acetone}/\text{H}_2/\text{He} = 10.8/1.8/67.3/20.0$. Catalysts reduced at 750°C .

3.5. Performance of the Ni, Co-Ni, and Co catalysts in the steam reforming of acetone

The results of acetone conversion in the homogeneous phase are provided in the Supplementary material (Fig. S5), together with the corresponding products formed as a function of reaction temperature. These experiments were performed using similar conditions of acetone flow and reactor volume as used for the catalytic reaction tests. The results showed that acetone decomposition became important at temperatures higher than about 620°C . The products of acetone decomposition were CH_4 , CO , and $\text{H}_2\text{C}=\text{CH}_2$, which are proposed to form via acetol [53]. The TPSR results for ethanol conversion are shown in Fig. 6, together with the composition of the SRA products, as a function of reaction temperature, for the Ni, Co-Ni, and Co catalysts reduced at 750°C . Fig. S-6 presents the TPSR results for ethanol conversion for catalysts reduced at 550°C .

The degree of metal reduction during the TPSR was evaluated using temperature-resolved XANES-SRA spectra collected at the Co and Ni K-edges of samples reduced at 750°C . After reduction, the samples were cooled under H_2 flow and at room temperature the flow of H_2 was replaced by the SRA mixture with $\text{H}_2\text{O}/\text{acetone}$ molar ratio of 6. Fitting of the XANES spectra was performed as described previously [44], resulting in the composition of NiO , Ni^0 , CoO , and Co^0 presented in Fig. 7. The results indicated that a fraction of Ni^0 or Co^0 was oxidized when the H_2 was replaced by the SRA mixture at room temperature.

The TPSR results showed that CO_2 was formed as the main product at temperatures in the range 250 – 300°C (Fig. 6). The XANES-SRA spectra (Fig. 7) indicated that in this temperature region, there were slight increases in the degree of reduction of NiO or CoO , suggesting that the metal oxides were reduced by acetone, forming CO and CO_2 . The relative rates of reduction and oxidation of Ni and Co by reactants determined the degree of oxidation. At temperatures near 350°C (Fig. 6), there was abrupt enhancement of formation of CO , CO_2 , and H_2 , and the XANES-SRA data indicated a higher degree of reduction of the catalysts. These results showed that at about 350°C , the reduction of the metal oxides by acetone was greater than oxidation of the metals by H_2O , suggesting that metal sites became predominant at the surface. At temperatures exceeding around 350°C , the higher rate of formation of H_2 and increased degree of reduction indicated that C–H bond cleavage and formation of H_2 was mainly catalyzed by metal sites. Possible reactions leading to the formation of CO and CO_2 were: (i) reduction of the metal oxides by acetone, and (ii) cleavage of the C–CO bond and subsequent oxidation reactions of intermediates of the reforming reaction (discussed below).

Increase of the reaction temperature, using an $\text{H}_2\text{O}/\text{acetone}$ molar ratio of 6 and catalysts containing Co, Co-Ni, or Ni reduced at 550°C (Fig. S6) or 750°C (Fig. 6), resulted in the formation of CH_4 . Although the fraction of CH_4 formed was low, relative to CO and CO_2 , it increased with the Ni content of the catalyst ($\text{Ni} > \text{Co-Ni}$). After total conversion of acetone, increasing the temperatures for

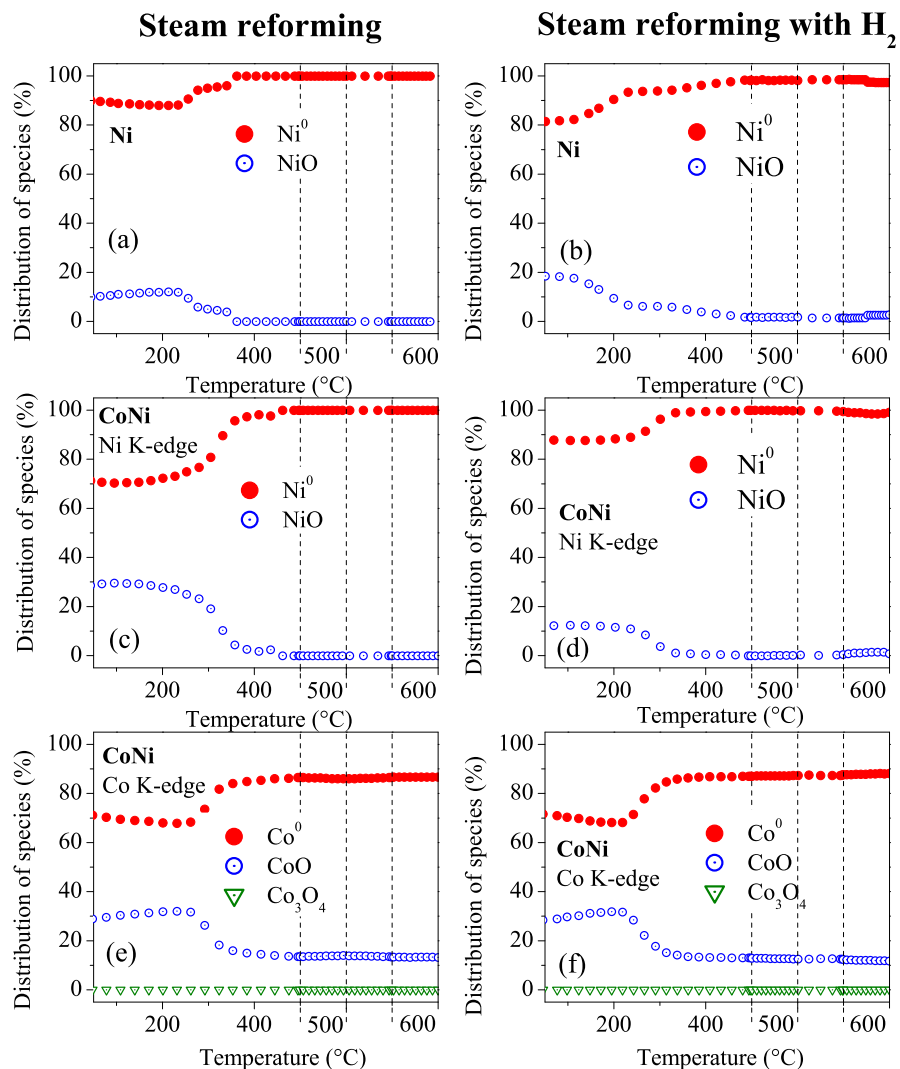


Fig. 7. Linear combination fitting during the SRA reaction, as a function of temperature, for reactor feeds with two compositions: (a) Ni and (c) Co-Ni catalysts at the Ni K-edge, and (e) Co-Ni catalyst at the Co K-edge, in SRA using $\text{H}_2\text{O}/\text{acetone}/\text{He} = 10.8/1.8/87.4$; (b) Ni and (d) Co-Ni catalysts at the Ni K-edge, and (e) Co-Ni catalyst at the Co K-edge, in SRA with addition of H_2 , using $\text{H}_2\text{O}/\text{acetone}/\text{H}_2/\text{He} = 10.8/1.8/67.4/20.0$. Catalysts reduced at 750°C .

heating the Ni and Co-Ni catalysts reduced at 750°C (Fig. 6a and c) resulted in the H_2 and CO_2 fractions reaching maxima, after which the CO_2 fraction decreased, followed by an increase of CO with temperature. These results suggested that the changes in CO and CO_2 composition were caused by an exothermic water gas shift reaction (WGSR) in quasi-equilibrium ($\text{CO} + \text{H}_2\text{O} \leftrightarrow \text{CO}_2 + \text{H}_2$). The Co, Co-Ni, and Ni catalysts reduced at the lower temperature of 550°C (Fig. S6) and the Co catalyst reduced at 750°C (Fig. 6e) showed anomalous behavior with respect to the changes expected in the CO and CO_2 fractions caused by the presence of the WGSR. This could have been due to strong interaction of NiO and CoO with the support, as demonstrated by the TPR results (Fig. S2). For the Ni, Co-Ni, and Co catalysts reduced at 550°C , and the Co catalyst reduced at 750°C , this strong interaction with the support reflected in the increase of degree of metal reduction during reaction at temperatures higher than about 550°C .

In order to obtain insight into the reaction pathways, the TPSR of SRA was performed with a high concentration of H_2 in the reactor feed (acetone/ $\text{H}_2\text{O}/\text{H}_2/\text{He} = 10.8/1.8/67.4/20.0$). The results for catalysts reduced at 750°C are shown in Fig. 6b, 6d and 6f. The detailed products distribution obtained at low temperatures is shown in Table 2. Interestingly, for the Ni catalysts, there was an abrupt increase in acetone conversion at about 230°C , which

was lower than the temperatures of around 330°C observed for the Co-containing catalysts (Co-Ni and Co). Comparison of acetone conversion over the Ni catalysts in the absence and presence of H_2 in the reactor feed (Fig. 6a and b, respectively) revealed that this increase in acetone conversion occurred at a temperature around 100°C lower in the presence of H_2 . The corresponding temperature-resolved XANES-SRA experiments (Fig. 7) demonstrated that with the Ni catalysts, the decrease of NiO fraction began at a lower temperature when H_2 was present in the feed. This suggests that the surfaces of the Ni catalysts oxidized in the presence of H_2O and at low temperatures were more easily reduced by H_2 than by acetone. The Ni^0 sites formed in the presence of H_2 catalyzed the acetone conversion. At low temperatures, acetaldehyde, acetic acid, and 2-propanol were detected as reaction products (Table 2). In the absence of H_2 , the reactions occurred at higher temperatures and the intermediate products were not detectable. The products formed in the presence of H_2 reflected the hydrogenation of some intermediates, and could contribute to understanding the reaction pathway.

Comparison of the TPRS and XANES-SRA results for the Co-Ni catalysts in the absence (Figs. 6 and 7 c-e) and presence (Figs. 6 and 7 d-f) of H_2 in the reactor feed indicated that the reduction of Co and Ni in the Co-Ni catalyst occurred in a similar temperature

Table 2

Acetone conversion and molar fractions of products from steam reforming at low temperatures with H₂ in the reactor feed. EtOH: ethanol; AcH: acetaldehyde; HAc: acetic acid; 2-PrOH: 2-propanol (isopropanol).

Temperature (°C)	Catalyst	Xacetone	CO	CH ₄	CO ₂	EtOH	AcH	HAc	2-PrOH
250	Ni	45.4	5.5	38.4	1.8	0.6	2.3	0.7	2.0
	Co-Ni	41.9	3.3	27.0	4.0	0.6	0	0.8	2.4
	Co	38.2	1.5	18.6	2.3	0.8	0	1.7	2.7
300	Ni	56.7	12.2	68.0	4.2	0	0.2	0.4	0.9
	Co-Ni	30.7	5.7	27.0	4.0	0.3	0.3	0	0.8
	Co	26.6	2.7	11.1	3.0	0	0	6.0	0.9
350	Ni	100	0.1	98.9	0.9	0	0	0	0
	Co-Ni	27.1	8.6	21.5	5.8	0	0	0	0.3
	Co	24.2	7.6	4.2	3.2	0	0	0	0.3

Table 3

Carbon accumulation rate. Conditions: P_{acetone} = 8.4 kPa; H₂O/acetone/He = 10.8/1.8/87.4; H₂O/acetone = 6; 4 h reaction at 500 or 600 °C.

Catalyst	r _{C(g-carbon/hg-catal.)} T = 500 °C	r _{C(g-carbon/hg-catal.)} T = 600 °C
Ni	1.94	0.43
Ni-Co	1.33	0.15
Co	0.61	0.04

region, independent of the presence of H₂. Different to the catalyst containing only Ni, the Co-Ni catalyst remained oxidized at low temperatures around 200 °C.

Interesting, the TPSR with the Ni catalysts (Fig. 6b), using H₂ in the feed, showed that at low temperatures of around 280 °C, the acetone was mainly converted to CH₄, indicating that the intermediates formed in the activation of acetone, with cleavage of the C–C bond, were hydrogenated to form CH₄. When the temperature was increased, CH₄ formation decreased, followed by an increase in CO formation. These results indicated that the intermediates formed in the activation of acetone were decomposed to H₂ and CO. It is therefore reasonable to suppose that some of the intermediates such as CH_x, CO, and C, formed in steam reforming of methane (CH₄ + H₂O ⇌ CO + 3H₂), were identical to those formed during SRA over Ni catalysts. For example, depending on temperature and atmosphere, CH_x species can be hydrogenated to CH₄ or decomposed to C and H₂. The increase in CH₄ formation in SRA with increasing Ni content (Fig. 6) could be indicative of the surface accumulation of CH_x species, which were more easily hydrogenated on the highly reduced Ni surface, relative to the Co-containing catalysts.

Table 3 gives the results for carbon accumulated during the evaluation of catalyst stability for 4 h on stream, using an H₂O/acetone reactant ratio of 6. After 4 h on stream, the carbon accumulation rate (r_C) decreased with increases in Co content and reaction temperature. Thermogravimetric analyses were performed after the 4 h on stream (Fig. S7). For samples used at 500 °C, the maximum carbon oxidation temperature decreased with an increase of the Co content, with values of 570, 500, and 420 °C for the Ni, Co-Ni, and Co catalysts, respectively. For samples used at 600 °C, the maximum carbon oxidation temperature was around 590 °C and slightly decreased with Co content. The high temperatures for coke oxidation were characteristic of whisker carbon. For the Ni catalysts, the higher temperatures were associated with oxidation, rather than catalysis. Oxidation has been reported to occur at 550 °C [54]. The decrease in carbon oxidation temperature with Co content was indicative of the formation of less organized carbon, and it is possible that the carbon oxidation was catalyzed by CoO.

4. Discussion

The parameters that control the activity and selectivity of metal nanoparticles in reforming reactions that involve reactants with oxi-reducing properties have been identified as the nature

of the metal and reactants, temperature, and metal particle size [6]. The changes in free energy during the oxidation reaction (metal + O ⇌ metal – O) depend on the curvature of the metal particle, reactant composition, and the nature of the metal [55]. Oxidation of the metal is favored by smaller particle size [46,55,56]. A specific metal nanoparticle surface adopts the structure corresponding to thermodynamic equilibrium, which can determine the activity and selectivity. The TPD of acetone adsorbed on reduced Ni, Co-Ni, and Co nanoparticles (Fig. 4) demonstrated that C–H cleavage, characterized by desorption of H₂, occurred at temperatures above 150 °C. However, in SRA the temperature for C–H cleavage and formation of H₂ depends on the reactant composition. For SRA on the Ni catalyst with and without H₂ in the reactor feed, H₂ was formed at temperatures above 200 and 350 °C, respectively.

This difference in temperatures for C–H cleavage could be explained from the experimental XAS results for the Ni and Co-Ni catalysts (Fig. 7), which demonstrated that the metal nanoparticles exposed to an acetone/H₂O mixture were partially oxidized by H₂O to NiO and CoO at low temperatures. In addition, the inability of the catalysts to cleave the C–H bond and form H₂ during acetone reforming at low temperatures suggests the presence of an oxide layer over a metal core. In a previous study [57], an initial NiO shell with thickness of about 3 nm was formed during oxidation of Ni particles with sizes between 9 and 96 nm. The reduction of oxides occurs at temperatures in which the rate of reduction by acetone or H₂ is predominant to the rate of oxidation of the metal by H₂O. The high density of metal sites on the surface confers the ability of the catalyst to reform acetone, with cleavage of the C–H and C–CO bonds of the acetone molecule. For the catalyst containing only Ni in the presence of H₂/acetone/H₂O, different to the catalyst in the presence of acetone/H₂O in the reactor feed, the XAS results indicated that the fraction of NiO decreased significantly at temperatures higher than about 200 °C.

The mechanisms of NiO reduction by H₂ and acetone should be considered. The reduction of oxides can be described by two kinetic models: the “nucleation model” and the “interface-controlled model” [57,58]. The interface-controlled kinetic model can be used to explain the reduction of our system of Ni⁰ core with NiO shell [57], where the reduction process occurred rapidly by H₂ adsorption and lowered the energy barrier associated with cleavage of the H–H bond over Ni⁰ sites. It is reasonable to suppose that the reduction of the NiO shell with acetone occurs via C–H cleavage over Ni⁰ sites. However, the adsorption energy and the energy barrier for bond cleavage are probably distinct for H₂ and acetone, resulting in different reduction temperatures. The wide temperature range to achieve a high degree of reduction of catalysts in reforming of acetone, with or without H₂, reflects the equilibrium between reduction of NiO by H₂ or acetone and oxidation by H₂O, with the reduction of NiO being favored at higher temperature.

In contrast to the Ni catalysts, the reduction temperatures of the oxides over the Co-containing catalysts (Co or Co-Ni) were similar for SRA in the presence or absence of H₂, indicating the high stability

of NiO and CoO on a Co–Ni core. Zonnevylle et al. [59] demonstrated that CoO is stabilized on Co nanoparticles. However, the mechanism of stabilization of CoO on Co-NPs is not fully understood, and the redox equilibrium on NPs may be governed by high kinetic barriers related to structural phase transformations. The stability is dependent on the electronic properties of the metal/oxide–metal pairs on the surface, which are determined by chemical composition and nanoparticle size [6]. The Ni, Co, and Co–Ni catalysts were partially oxidized, with the degree of oxidation decreasing with temperature in the presence of H_2O and H_2 in the reactor feed. The presence of 2-propanol as a reaction product at low temperatures (Table 2) indicated that oxides catalyzed the hydrogenation of acetone. However, Co-containing catalysts with higher fractions of CoO showed the formation of acetic acid at low temperatures (Table 2), suggesting the oxidation of intermediates due to the presence of this metal oxide.

Scheme 1 summarizes probable reaction pathways in SRA over Co and Ni catalysts, based on the experimental results and the literature data, as discussed below.

The adsorption of acetone (CH_3COCH_3) on the metal surface is favored for the $\eta^2(\text{C},\text{O})$ configuration [38], with activation of acetone by scission of the C–C, C–O, or C–H bonds. DFT calculations [41] have demonstrated that for acetone activation on Co nanoparticles ($\approx 5\text{ nm}$), the energy barriers (ΔE) associated with cleavage of C–C bond, together with the corresponding reaction enthalpies (ΔH), are larger for demethylation to form $\text{CH}_3\text{CO}^* + * \text{CH}_3$ ($\Delta E = 0.78\text{ eV}$; $\Delta H = -0.22\text{ eV}$) or deoxygenation to form $\text{CH}_3\text{CCH}_3^* + \text{O}^*$ ($\Delta E = 1.65\text{ eV}$; $\Delta H = -0.63\text{ eV}$) than for cleavage of the C–H bond to form $\text{CH}_3\text{COCH}_2^* + \text{H}^*$ ($\Delta E = 0.34\text{ eV}$; $\Delta H = -0.72\text{ eV}$) (step 1A in Scheme 1). The next consecutive steps are dehydrogenation of $\text{CH}_3\text{COCH}_2^*$ species form CH_3COCH^* and CH_3COC^* or $\text{C}-\text{CH}_2$, where the last species is formed by scission of $\text{CH}_3\text{COCH}_2^*$, and show very high barriers of 1.08, 1.21, and 1.11 eV [38], respectively. These consecutive dehydrogenation reactions of $\text{CH}_3\text{COCH}_2^*$, calculated using a four-layer-thick slab of 3×3 Co(111) surface cells, are highly endothermic, with ΔH of 0.73, 0.61, and 0.87 eV, respectively [38]. The hydrogenation of $\text{CH}_3\text{COCH}_2^*$ to give $\text{CH}_3\text{COCH}_3^*$ (step 2A in Scheme 1) shows $\Delta E = 0.64\text{ eV}$ and $\Delta H = 0.42\text{ eV}$, [38] and is favored relative to dehydrogenation of $\text{CH}_3\text{COCH}_2^*$ (step 3A in Scheme 1), while acetaldehyde is one of the products of reaction on Ni catalysts at low temperature (Table 2). FTIR analysis of acetone adsorbed on Ni catalysts in the presence of H_2 showed bands associated with acetyl species on the metal surface, indicating the hydrogenation of CH_3CO^* species.

These results strongly suggest that the reactions for decomposition of acetone via scission of $\text{CH}_3\text{COCH}_3^*$ to $\text{CH}_3\text{CO}^* + \text{CH}_3^*$ (step 2 and 2A in Scheme 1), at higher temperatures, may be favored relative to consecutive steps of dehydrogenation of $\text{CH}_3\text{COCH}_2^*$ (steps 1A and 3A in Scheme 1, respectively). However, it is worth noting that acetone activation via demethylation to form $\text{CH}_3\text{CO}^* + * \text{CH}_3$ (step 2 in Scheme 1) is sensitive to structure, since it is favored on Co nanoparticles ($\approx 5\text{ nm}$) ($\Delta E = 0.78\text{ eV}$; $\Delta H = -0.22\text{ eV}$) [41], but is not favored on a Co(111) surface ($\Delta E = 0.69\text{ eV}$; $\Delta H = 0.44\text{ eV}$) [38]. DFT studies of the decomposition of the acetyl intermediate (CH_3CO^*) via C–C, C–O, or β –C–H bond scission over Co have given ΔE values of 0.79, 0.79, and 0.59 eV, and ΔH values of -0.4 , -0.37 , and 0.48 eV , respectively, suggesting that the decomposition of CH_3CO^* species probably occurs via scission of C–C and C–O bonds.

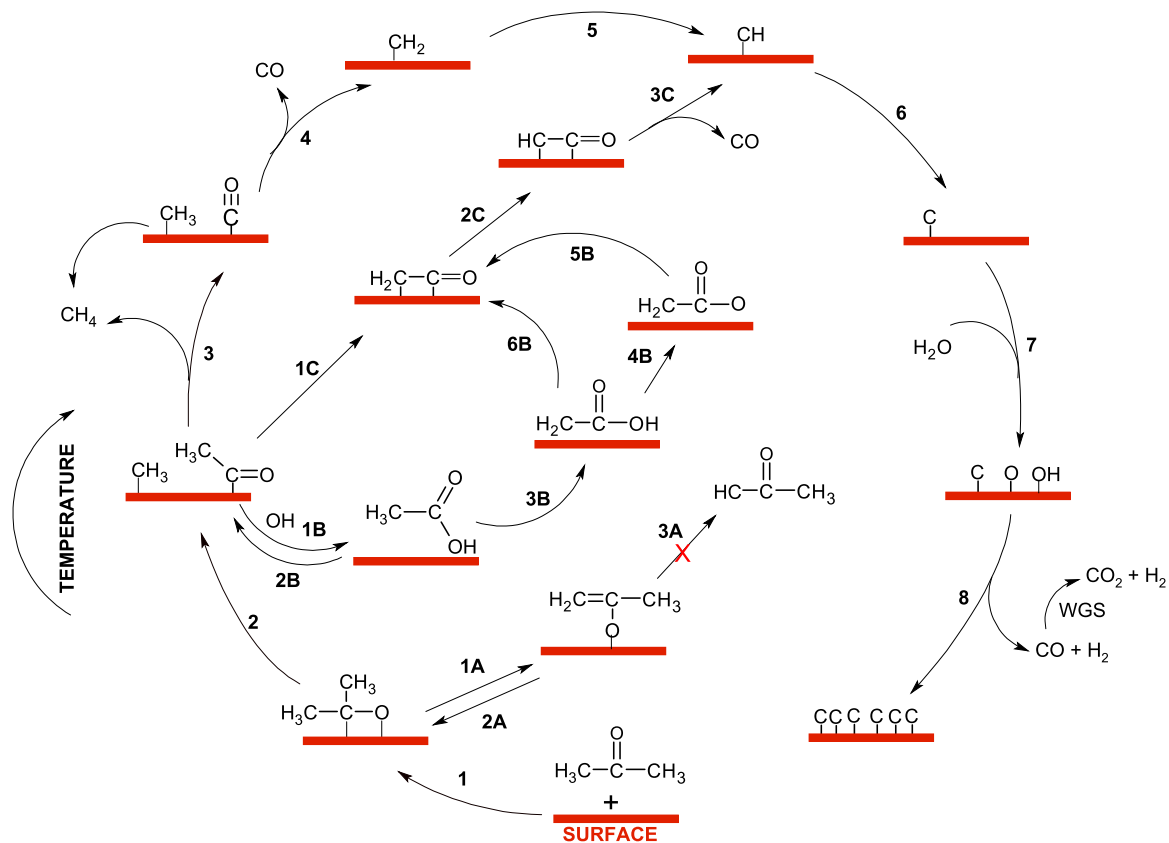
The TPD results showed that the H_2 and CO desorption peak maxima occurred at similar temperatures, and indicated that scission of the C–H bond of different intermediates was very fast and in the same temperature region as C–CO bond scission. Acetic acid was observed amongst the SRA products, especially for the Co catalyst at low temperature (Table 2). It should be noted that the surfaces of the metal nanoparticles in Ni, Co–Ni, and Co cata-

lysts are oxidized in SRA at low temperature. The data indicated that NiO, CoO, and OH species can probably promote a reforming route via oxidation of CH_3CO^* species ($\text{CH}_3\text{CO}^* + \text{OH}^* \rightarrow \text{CH}_3\text{COOH}^*$, (step 1B in Scheme 1). In a DFT study of acetic acid conversion over Co stepped surface, Li et al. [38] identified four potential relevant reaction routes for acetic acid decomposition. Two of the routes, involving reduction with formation of CH_3CO^* species, are reverse reactions of the formation of acetic acid shown above. The other two routes are via dehydrogenation of acetic acid: (i) $\text{CH}_3\text{COOH}^* \rightarrow \text{CH}_2\text{COOH}^* \rightarrow \text{CH}_2\text{COO}^* \rightarrow \text{CH}_2\text{CO}^*$ (steps 3B, 4B, and 5B in Scheme 1), and (ii) $\text{CH}_3\text{COOH}^* \rightarrow \text{CH}_2\text{COOH}^* \rightarrow \text{CH}_2\text{CO}^*$ (steps 3B and 6B in Scheme 1). Elsewhere, DFT calculations have shown that ethanol conversion over Co and Ni can occur via acetyl (CH_3CO^*) species [6,60], similar to the decomposition of acetone, which is converted by successive dehydrogenation to $^*\text{CH}_2\text{C}^*\text{O}$ and $^*\text{CHC}^*\text{O}$ (steps 1C and 2C in Scheme 1). The scission of C–C bond is favored from the $^*\text{CHC}^*\text{O}$ intermediate, giving methylidyne ($^*\text{CH}$) and $^*\text{CO}$ as products (step 3C in Scheme 1) [61].

From the experimental data and the literature DFT values, it is therefore reasonable to propose that the reaction pathway for the reforming of acetone over catalysts containing Co and/or Ni involves two main routes: (i) activation of acetone to give $^*\text{CH}_3$ and $^*\text{CH}_3\text{CO}$ species (steps 1–2 in Scheme 1), followed by decomposition of $^*\text{CH}_3\text{CO}$ to give $^*\text{CH}_3$ and $^*\text{CO}$ (step 3 in Scheme 1); and (ii) successive dehydrogenation of $^*\text{CH}_3\text{CO}$ to give $^*\text{CH}$ and $^*\text{CO}$ (steps 1C–3C in Scheme 1).

The products formed in TPSR were strongly dependent on the reactor feed composition. For the Ni catalyst, the presence of H_2 in the feed at low temperatures resulted in the formation of CH_4 as the main product. The decomposition of CH_x^* species on Ni was calculated by Jones et al. [45], considering that the first step of dehydrogenation of the CH_3^* species was endothermic and that the consecutive dehydrogenation steps were exothermic. The various dehydrogenation steps showed ΔE values favorable for the reaction to occur. Here, the TPSR and XAS experiments demonstrated that for the Ni catalyst with H_2 in the reactor feed, the fraction of Ni oxidized decreased at low temperatures and the catalysts became very active for formation of CH_4 alone. For SRA over Ni catalysts, the $^*\text{CH}_x$ species could be formed by C–C bond scission of acetone (steps 2–5 in Scheme 1) and ketenyl ($^*\text{CHC}^*\text{O}$) (step 3C in Scheme 1). At low temperatures, the hydrogenation reaction of $^*\text{CH}_x$ species to CH_4 is exothermic. For the Co and Co–Ni catalysts, the TPSR and XAS results showed that with H_2 in the reactor feed, the activities of the catalysts were very low at low temperatures, and that there was a degree of oxidized Ni and Co. The Co and Co–Ni catalysts only became able to activate acetone at high temperatures (320°C) after reduction of CoO and NiO species on the metal core. However, at high temperatures, the hydrogenation of CH_3^* species to CH_4 was not favorable, relative to decomposition of CH_3^* . The reaction pathway changed, with decomposition of CH_x species instead of hydrogenation to CH_4 . The dehydrogenation of CH_x^* species was favored by higher temperatures, leading to a pyrolytic pathway with formation of carbon (steps 4–6 in Scheme 1) [45]. The free energy of the CH_3^* species was similar for Ni and Co, and the free energies of O^* and OH^* were negative for Co and positive for Ni [45]. This suggests that similar concentrations of CH_3^* species would be expected over Ni or Co, and that very high concentrations of O^* and OH^* species would occur on Co, compared to a Ni surface. The significant decrease of CH_4 formation for the Co catalyst, relative to Co–Ni, could therefore be attributed to higher fractions of O^* and OH^* species on the Co catalyst than on Co–Ni. The existence of CoO and O^* adatoms over a Co surface could hinder the hydrogenation reaction to form CH_4 .

The accumulation of carbon depended on the Ni/Co composition and the reaction temperatures (Table 3). Although $^*\text{CH}_x$ could be oxidized to CO_2 by $^*\text{OH}$ species, DFT calculations for the reaction



Scheme 1. Representation of the SRA Reaction Pathways as a Function of Temperature. Abstracted H* atoms are omitted.

on a Co (0001) surface indicated that the first step of this reaction (${}^*\text{CH}_3 + {}^*\text{OH} \rightarrow \text{H}_3\text{CO}^* + {}^*\text{H}$) was not kinetically favored [62]. The accepted mechanism for oxidation of ${}^*\text{CH}_x$ is via dehydrogenation, forming ${}^*\text{C}$ and H₂, followed by ${}^*\text{C}$ oxidation by ${}^*\text{O}$ or ${}^*\text{OH}$ species (step 8 in Scheme 1). Nevertheless, the accumulation of ${}^*\text{C}$ on the surface depends on the relative rates of ${}^*\text{C}$ formation and oxidation. The free energy of O and OH species was found to be lower for Co than for Ni [45], indicating higher density of O and OH on Co-based catalysts, in agreement with the XAS results that demonstrated a higher degree of oxidation (CoO) in Co-containing catalysts, relative to the Ni catalyst. The strong decrease of C accumulation for Co-containing catalysts could be attributed to higher reaction rates for oxidation of ${}^*\text{C}$ by O and OH, and the presence of CoO on the metal cores of the Co [44] and Co-Ni catalysts.

The in situ characterization results discussed above suggest that the degree of oxidation of metal nanoparticles and the reaction temperature are crucial for determining the reaction pathway and for controlling CH₄ formation and carbon accumulation. Our results indicate that the reactivity of Ni towards oxygen at low temperatures can be adjusted by tuning the electronic properties by means of alloy formation and decreasing the metal particle size. Ni-based catalysts are probable candidates for industrial use in the steam reforming of biomass-derived compounds. However, the development of catalysts that are stable at high temperatures under reactant mixtures is an issue that remains to be resolved. It is necessary to identify suitable formulations, methods of preparation, and activation procedures, as well as to understand the dynamics of reduction/oxidation of catalysts during reactions.

5. Conclusions

Co- and Ni-based catalysts were partially oxidized in contact with SRA reaction mixtures (acetone/H₂O) at room temperature.

The thermodynamic equilibrium for reduction of the oxidized surface strongly depended on temperature, the nature of the metal, and the redox potentials of the reactants. The reduction of NiO indicated the presence of oxygen vacancies on NiO–Ni core shell-like nanoparticles, which were able to cleave H₂, with subsequent reduction of NiO. The Ni nanoparticles became reduced and active for acetone conversion in the presence of acetone/H₂ at low temperature (200 °C), while the Co nanoparticles were only reduced at high temperature (300 °C) in the presence of acetone with or without H₂.

The reaction pathway was strongly influenced by reduction of the Co-Ni nanoparticle surface. In the presence of H₂, the Ni catalyst was reduced at low temperatures (200–300 °C) and active for cleavage of the C–C bond of acetone. Nevertheless, the fragments formed in the C–C scission were hydrogenated to CH₄ and the SRA was not possible at low temperatures over the Ni catalyst. Increase of the reaction temperature resulted in the CH_x fragments formed in the acetone activation being dehydrogenated to produce ${}^*\text{C}$ and H₂.

The surfaces of the Co-containing catalysts remained oxidized and inactive at low temperatures (<300 °C). At high temperatures, the metal oxides at the surface were reduced and the catalysts became active for dehydrogenation of ${}^*\text{CH}_x$ species, while the hydrogenation of ${}^*\text{CH}_x$ to CH₄ was not favored at high temperatures. The strong decrease in C accumulation for the Co-containing catalysts could be explained by the higher reaction rates for oxidation of ${}^*\text{C}$ by O and OH, as well as the presence of CoO on the metal cores of the Co and Co-Ni catalysts.

Acknowledgements

The authors are grateful for the financial support provided by Fundação de Amparo à Pesquisa do Estado de São Paulo (FAPESP,

process 2011-50727-9 and 2013/10858-2), Conselho Nacional de Desenvolvimento Científico e Tecnológico (CNPq, Project FNI E02/16), the Brazilian Synchrotron Light Laboratory (LNLS) for use of DXAS beamline (proposal XAFS1-16215) and Brazilian Nanotechnology National Laboratory for the use of TEM facilities (proposal TEM-18527). The authors also gratefully acknowledge the fruitful discussions held with their students and co-workers.

Appendix A. Supplementary data

Supplementary data associated with this article can be found, in the online version, at <http://dx.doi.org/10.1016/j.apcatb.2016.04.047>.

References

- [1] J.A. Turner, A realizable renewable energy future, *Science* 285 (1999) 687–689, <http://dx.doi.org/10.1126/science.285.5428.687>.
- [2] P.K. Cheekatamarla, C.M. Finnerty, Reforming catalysts for hydrogen generation in fuel cell applications, *J. Power Sources* 160 (2006) 490–499, <http://dx.doi.org/10.1016/j.jpowsour.2006.04.078>.
- [3] A. Oasmaa, D. Meier, Norms and standards for fast pyrolysis liquids, *J. Anal. Appl. Pyrolysis* 73 (2005) 323–334, <http://dx.doi.org/10.1016/j.jaap.2005.03.003>.
- [4] D. Chen, L. He, Towards an efficient hydrogen production from biomass: a review of processes and materials, *ChemCatChem* 3 (2011) 490–511, <http://dx.doi.org/10.1002/cctc.201000345>.
- [5] F. Bimbela, M. Oliva, J. Ruiz, L. García, J. Arauzo, Hydrogen production by catalytic steam reforming of acetic acid, a model compound of biomass pyrolysis liquids, *J. Anal. Appl. Pyrolysis* 79 (2007) 112–120, <http://dx.doi.org/10.1016/j.jaap.2006.11.006>.
- [6] D. Zanchet, J.B.S. Oliveira, J.M.R. Gallo, S. Damyanova, J.M.C. Bueno, Towards Understanding Metal-Catalyzed Ethanol Reforming 5 (6) (2015) 3841–3863, <http://dx.doi.org/10.1021/cs5020755>.
- [7] R. Gui-Lopez, R.M. Navarro, A.A. Ismail, S.A. Al-Sayari, J.L.G. Fierro, Influence of Ni environment on the reactivity of Ni–Mg–Al catalysts for the acetone steam reforming reaction, *Int. J. Hydrogen Energy* 40 (2015) 5289–5296, <http://dx.doi.org/10.1016/j.ijhydene.2015.01.159>.
- [8] X. Hu, L. Zhang, G. Lu, Pruning of the surface species on Ni/Al₂O₃ catalyst to selective production of hydrogen via acetone and acetic acid steam reforming, *Appl. Catal. A* 427–428 (2012) 49–57, <http://dx.doi.org/10.1016/j.apcata.2012.03.029>.
- [9] L.V. Mattos, G. Jacobs, B.H. Davis, F.B. Noronha, Production of hydrogen from ethanol: review of reaction mechanism and catalyst deactivation, *Chem. Rev.* 112 (2012) 4094–4123, <http://dx.doi.org/10.1021/cr2000114>.
- [10] X. Hu, G. Lu, Investigation of the steam reforming of a series of model compounds derived from bio-oil for hydrogen production, *Appl. Catal. B* 88 (2009) 376–385, <http://dx.doi.org/10.1016/j.apcatb.2008.10.021>.
- [11] J.R. Galdámez, L. García, R. Bilbao, Hydrogen production by steam reforming of bio-oil using coprecipitated Ni–Al catalysts. Acetic acid as a model compound, *Energy Fuels* 19 (2005) 1133–1142, <http://dx.doi.org/10.1021/ef049718g>.
- [12] M. Marquevich, S. Czernik, E. Chornet, D. Montané, Hydrogen from biomass: steam reforming of model compounds of fast-pyrolysis oil, *Energy Fuels* 13 (1999) 1160–1166, <http://dx.doi.org/10.1021/ef990034w>.
- [13] C. Rioche, S. Kulkarni, F.C. Meunier, J.P. Breen, R. Burch, Steam reforming of model compounds and fast pyrolysis bio-oil on supported noble metal catalysts, *Appl. Catal. B* 61 (2005) 130–139, <http://dx.doi.org/10.1016/j.apcatb.2005.04.015>.
- [14] D. Wang, D. Montané, E. Chornet, Catalytic steam reforming of biomass-derived oxygenates: acetic acid and hydroxyacetaldehyde, *Appl. Catal. A* 143 (1996) 245–270, [http://dx.doi.org/10.1016/0926-860X\(96\)00093-2](http://dx.doi.org/10.1016/0926-860X(96)00093-2).
- [15] A.C. Basagiannis, X.E. Verykios, Reforming reactions of acetic acid on nickel catalysts over a wide temperature range, *Appl. Catal. A* 308 (2006) 182–193, <http://dx.doi.org/10.1016/j.apcata.2006.04.024>.
- [16] P.N. Kechagiopoulos, S.S. Voutetakis, A.A. Lemonidou, I.A. Vasalos, Hydrogen production via steam reforming of the aqueous phase of bio-oil in a fixed bed reactor, *Energy Fuels* 20 (2006) 2155–2163, <http://dx.doi.org/10.1021/ef060083q>.
- [17] A.C. Basagiannis, X.E. Verykios, Catalytic steam reforming of acetic acid for hydrogen production, *Int. J. Hydrogen Energy* 32 (2007) 3343–3355, <http://dx.doi.org/10.1016/j.ijhydene.2007.04.039>.
- [18] A.C. Basagiannis, X.E. Verykios, Steam reforming of the aqueous fraction of bio-oil over structured Ru/MgO/Al₂O₃ catalysts, *Catal. Today* 127 (2007) 256–264, <http://dx.doi.org/10.1016/j.cattod.2007.03.025>.
- [19] F. Bimbela, M. Oliva, J. Ruiz, L. García, J. Arauzo, Catalytic steam reforming of model compounds of biomass pyrolysis liquids in fixed bed: acetal and n-butanol, *J. Anal. Appl. Pyrolysis* 85 (2009) 204–213, <http://dx.doi.org/10.1016/j.jaap.2008.11.033>.
- [20] T. Davidian, N. Guilhaume, E. Ilojou, H. Provendier, C. Mirodatos, Hydrogen production from crude pyrolysis oil by a sequential catalytic process, *Appl. Catal. B* 73 (2007) 116–127, <http://dx.doi.org/10.1016/j.apcatb.2006.06.014>.
- [21] E. Vagia, A. Lemonidou, Thermodynamic analysis of hydrogen production via steam reforming of selected components of aqueous bio-oil fraction, *Int. J. Hydrogen Energy* 32 (2007) 212–223, <http://dx.doi.org/10.1016/j.ijhydene.2006.08.021>.
- [22] C. Wu, R. Liu, Sustainable hydrogen production from steam reforming of bio-oil model compound based on carbon deposition/elimination, *Int. J. Hydrogen Energy* 36 (2011) 2860–2868, <http://dx.doi.org/10.1016/j.ijhydene.2010.11.113>.
- [23] C.-F. Yan, F.-F. Cheng, R.-R. Hu, Hydrogen production from catalytic steam reforming of bio-oil aqueous fraction over Ni/CeO₂–ZrO₂ catalysts, *Int. J. Hydrogen Energy* 35 (2010) 11693–11699, <http://dx.doi.org/10.1016/j.ijhydene.2010.08.083>.
- [24] P.J. Ortiz-Toral, J. Satrio, R.C. Brown, B.H. Shanks, Steam reforming of bio-oil fractions: effect of composition and stability, *Energy Fuels* 25 (2011) 3289–3297, <http://dx.doi.org/10.1021/ef200628q>.
- [25] K.K. Pant, P. Mohanty, S. Agarwal, A.K. Dalai, Steam reforming of acetic acid for hydrogen production over bifunctional Ni–Co catalysts, *Catal. Today* 207 (2013) 36–43, <http://dx.doi.org/10.1016/j.cattod.2012.06.021>.
- [26] A. Remiro, B. Valle, A.T. Aguayo, J. Bilbao, A.G. Gayubo, Operating conditions for attenuating Ni/Al₂O₃– α Al₂O₃ catalyst deactivation in the steam reforming of bio-oil aqueous fraction, *Fuel Process. Technol.* 115 (2013) 222–232, <http://dx.doi.org/10.1016/j.fuproc.2013.06.003>.
- [27] S. Wang, Q. Cai, F. Zhang, X. Li, L. Zhang, Z. Luo, Hydrogen production via catalytic reforming of the bio-oil model compounds: acetic acid, phenol and hydroxyacetone, *Int. J. Hydrogen Energy* 39 (2014) 18675–18687, <http://dx.doi.org/10.1016/j.ijhydene.2014.01.142>.
- [28] V. Paasikallio, J. Kihlman, C.A.S. Sánchez, P. Simell, Y. Solantausta, J. Lehtonen, Steam reforming of pyrolysis oil aqueous fraction obtained by one-step fractional condensation, *Int. J. Hydrogen Energy* 40 (2015) 3149–3157, <http://dx.doi.org/10.1016/j.ijhydene.2015.01.025>.
- [29] M.V. Gil, J. Fermoso, F. Rubiera, D. Chen, H₂ production by sorption enhanced steam reforming of biomass-derived bio-oil in a fluidized bed reactor: an assessment of the effect of operation variables using response surface methodology, *Catal. Today* 242 (2015) 19–34, <http://dx.doi.org/10.1016/j.cattod.2014.04.018>.
- [30] R. Trane-Restrup, A.D. Jensen, Steam reforming of cyclic model compounds of bio-oil over Ni-based catalysts: product distribution and carbon formation, *Appl. Catal. B* 165 (2015) 117–127, <http://dx.doi.org/10.1016/j.apcatb.2014.09.026>.
- [31] R.M. Navarro, R. Gui-Lopez, J.M. Gonzalez-Carballo, A. Cubero, A.A. Ismail, S.A. Al-Sayari, et al., Bimetallic MnNi/Al₂O₃–La catalysts (M=Pt, Cu) for acetone steam reforming: role of M on catalyst structure and activity, *Appl. Catal. A* 474 (2014) 168–177, <http://dx.doi.org/10.1016/j.apcata.2013.09.056>.
- [32] F. Bimbela, M. Oliva, J. Ruiz, L. García, J. Arauzo, Hydrogen production via catalytic steam reforming of the aqueous fraction of bio-oil using nickel-based coprecipitated catalysts, *Int. J. Hydrogen Energy* 38 (2013) 14476–14487, <http://dx.doi.org/10.1016/j.ijhydene.2013.09.038>.
- [33] R.M. Navarro, R. Gui-Lopez, A.A. Ismail, S.A. Al-Sayari, J.L.G. Fierro, Ni- and PtNi-catalysts supported on Al₂O₃ for acetone steam reforming: effect of the modification of support with Ce, La and Mg, *Catal. Today* 242 (2015) 60–70, <http://dx.doi.org/10.1016/j.cattod.2014.07.036>.
- [34] D. Yao, C. Wu, H. Yang, Q. Hu, M.A. Nahil, H. Chen, et al., Hydrogen production from catalytic reforming of the aqueous fraction of pyrolysis bio-oil with modified Ni–Al catalysts, *Int. J. Hydrogen Energy* 39 (2014) 14642–14652, <http://dx.doi.org/10.1016/j.ijhydene.2014.07.077>.
- [35] B. Matas Güell, I.M.T. da Silva, K. Seshan, L. Lefferts, Sustainable route to hydrogen—design of stable catalysts for the steam gasification of biomass related oxygenates, *Appl. Catal. B* 88 (2009) 59–65, <http://dx.doi.org/10.1016/j.apcatb.2008.09.018>.
- [36] B. Valle, B. Aramburu, A. Remiro, J. Bilbao, A.G. Gayubo, Effect of calcination/reduction conditions of Ni/Al₂O₃– α Al₂O₃ catalyst on its activity and stability for hydrogen production by steam reforming of raw bio-oil/ethanol, *Appl. Catal. B* 147 (2014) 402–410, <http://dx.doi.org/10.1016/j.apcatb.2013.09.022>.
- [37] E. Salehi, F.S. Azad, T. Harding, J. Abedi, Production of hydrogen by steam reforming of bio-oil over Ni/Al₂O₃ catalysts: effect of addition of promoter and preparation procedure, *Fuel Process. Technol.* 92 (2011) 2203–2210, <http://dx.doi.org/10.1016/j.fuproc.2011.07.002>.
- [38] X. Li, S. Wang, Y. Zhu, G. Yang, P. Zheng, DFT study of bio-oil decomposition mechanism on a Co stepped surface: acetic acid as a model compound, *Int. J. Hydrogen Energy* 40 (2015) 330–339, <http://dx.doi.org/10.1016/j.ijhydene.2014.11.004>.
- [39] J.W.C. Liberatori, R.U. Ribeiro, D. Zanchet, F.B. Noronha, J.M.C. Bueno, Steam reforming of ethanol on supported nickel catalysts, *Appl. Catal. A* 327 (2007) 197–204, <http://dx.doi.org/10.1016/j.apcata.2007.05.010>.
- [40] R.U. Ribeiro, J.W.C. Liberatori, H. Winnishofer, J.M.M. Bueno, D. Zanchet, Colloidal Co nanoparticles supported on SiO₂: synthesis, characterization and catalytic properties for steam reforming of ethanol, *Appl. Catal. A* 91 (2009) 670–678, <http://dx.doi.org/10.1016/j.apcatb.2009.07.009>.
- [41] J. Sun, D. Mei, A.M. Karim, A.K. Datye, Y. Wang, Minimizing the formation of coke and methane on Co nanoparticles in steam reforming of biomass-derived oxygenates, *ChemCatChem* 5 (2013) 1299–1303, <http://dx.doi.org/10.1002/cctc.201300041>.

[42] R. Alcalá, M. Mavrikakis, J.A. Dumesic, DFT studies for cleavage of CC and CO bonds in surface species derived from ethanol on Pt(111), *J. Catal.* 218 (2003) 178–190, [http://dx.doi.org/10.1016/S0021-9517\(03\)00090-3](http://dx.doi.org/10.1016/S0021-9517(03)00090-3).

[43] S. Andonova, C.N. De Ávila, K. Arishtirova, J.M.C. Bueno, S. Damyanova, Structure and redox properties of Co promoted Ni/Al₂O₃ catalysts for oxidative steam reforming of ethanol, *Appl. Catal. B* 105 (2011) 346–360, <http://dx.doi.org/10.1016/j.apcatb.2011.04.029>.

[44] C.N. Ávila-Neto, J.W.C. Liberatori, A.M. da Silva, D. Zanchet, C.E. Hori, F.B. Noronha, J.M.C. Bueno, Understanding the stability of Co-supported catalysts during ethanol reforming as addressed by *in situ* temperature and spatial resolved XAFS analysis, *J. Catal.* 287 (2012) 124–137, <http://dx.doi.org/10.1016/j.jcat.2011.12.013>.

[45] G. Jones, J. Jakobsen, S. Shim, J. Kleis, M. Andersson, J. Rossmeisl, F. Abild-Pedersen, T. Bligaard, S. Helveg, B. Hinnemann, J.R. Rostrup-Nielsen, I. Sehested, J. Chorkendorff, J.K. Nørskova, First principles calculations and experimental insight into methane steam reforming over transition metal catalysts, *J. Catal.* 259 (2008) 147–160, <http://dx.doi.org/10.1016/j.jcat.2008.08.003>.

[46] E. van Steen, M. Claeys, M.E. Dry, J. van de Loosdrecht, E.L. Viljoen, J.L. Visagie, Stability of nanocrystals: thermodynamic analysis of oxidation and re-reduction of cobalt in water/hydrogen mixtures, *J. Phys. Chem. B* 109 (2005) 3575–3577, <http://dx.doi.org/10.1021/jp045136o>.

[47] C.N. Ávila-Neto, D. Zanchet, C.E. Hori, R.U. Ribeiro, J.M.C. Bueno, Interplay between particle size, composition, and structure of MgAl₂O₄-supported Co–Cu catalysts and their influence on carbon accumulation during steam reforming of ethanol, *J. Catal.* 307 (2013) 222–237, <http://dx.doi.org/10.1016/j.jcat.2013.07.025>.

[48] J.A. Rodriguez, J.C. Hanson, A.I. Frenkel, J.Y. Kim, M. Pérez, Experimental and theoretical studies on the reaction of H₂ with NiO: role of O vacancies and mechanism for oxide reduction, *J. Am. Chem. Soc.* 124 (2002) 346–354, <http://dx.doi.org/10.1021/ja012108o>.

[49] G. Jacobs, Y. Ji, B.H. Davis, D. Cronauer, A.J. Kropf, C.L. Marshall, Fischer–Tropsch synthesis: temperature programmed EXAFS/XANES investigation of the influence of support type, cobalt loading, and noble metal promoter addition to the reduction behavior of cobalt oxide particles, *Appl. Catal. A* 333 (2007) 177–191, <http://dx.doi.org/10.1016/j.apcata.2007.07.027>.

[50] J.T. Richardson, M. Lei, B. Turk, K. Forster, M.V. Twigg, Reduction of model steam reforming catalysts: NiO/α-Al₂O₃, *Appl. Catal. A Gen.* 110 (2) (1994) 217–237.

[51] Wee-Sun Sim, Ting-Cheng Li, Peng-Xiang Yang, Boon-Siang Yeo, Isolation and identification of surface-bound acetone enolate on Ni(111), *J. Am. Chem. Soc.* 124 (2002) 4970–4971, <http://dx.doi.org/10.1021/ja025749j>.

[52] H. Zhao, J. Kim, E. Koel Bruce, Adsorption and reaction of acetaldehyde on Pt(111) and Sn/Pt(111) surface alloys, *Surf. Sci.* 538 (2003) 147–159, [http://dx.doi.org/10.1016/S0039-6028\(03\)00602-2](http://dx.doi.org/10.1016/S0039-6028(03)00602-2).

[53] F.O. Rice, R.E. Vorrath, The thermal decomposition of acetone in the gaseous state, *PNAS* 15 (1929) 702, <http://www.pnas.org/content/15/9/702.full.pdf?sid=c781aa11-496f-479c-8afe-954a9976cd85>.

[54] C. Li, T.C. Brown, Temperature-programmed oxidation of coke deposited by 1-octene on cracking catalysts, *Energy Fuels* 13 (1999) 888–894, <http://dx.doi.org/10.1021/ef980265n>.

[55] X. Lai, D.W. Goodman, Structure–reactivity correlations for oxide-supported metal catalysts: new perspectives from STM, *J. Mol. Catal. A: Chem.* 162 (2000) 33–50, [http://dx.doi.org/10.1016/S1381-1169\(00\)00320-4](http://dx.doi.org/10.1016/S1381-1169(00)00320-4).

[56] A. Saib, A. Borgna, J. Vandeloosdrecht, P. Vanberge, J. Geus, J. Niemantsverdriet, Preparation and characterisation of spherical Co/SiO₂ model catalysts with well-defined nano-sized cobalt crystallites and a comparison of their stability against oxidation with water, *J. Catal.* 239 (2006) 326–339, <http://dx.doi.org/10.1016/j.jcat.2006.02.004>.

[57] J.G. Railsback, A.C. Johnston-Peck, J. Wang, J.B. Tracy, Size-dependent nanoscale kirkendall effect during the oxidation of nickel nanoparticles, *ACS Nano* 4 (2010) 1913–1920, <http://dx.doi.org/10.1021/nn901736y>.

[58] L. Gao, C. Pang, D.F. He, J.M. Shen, A. Gupta, N.Z. Bao, Synthesis of hierarchical nanoporous microstructures via the kirkendall effect in chemical reduction process, *Sci. Rep.* 5 (2015) 16061, <http://dx.doi.org/10.1038/srep16061>.

[59] M.C. Zonnevylle, J.J.C. Geerlings, R.A. van Santen, Conversion of surface carbide to subsurface carbon on cobalt (0001): a theoretical study, *Surf. Sci.* 240 (1990) 253–262, [http://dx.doi.org/10.1016/0039-6028\(90\)90746-U](http://dx.doi.org/10.1016/0039-6028(90)90746-U).

[60] J.E. Sutton, D.G. Vlachos, Ethanol activation on closed-packed surfaces, *Ind. Eng. Chem. Res.* 54 (2015) 4213–4225, <http://dx.doi.org/10.1021/ie5043374>.

[61] J.E. Sutton, P. Panagiotopoulou, X.E. Verykios, D.G. Vlachos, Combined DFT, microkinetic, and experimental study of ethanol steam reforming on Pt, *J. Phys. Chem. C* 117 (2013) 4691–4706, <http://dx.doi.org/10.1021/jp312593u>.

[62] Y. Ma, L. Hernandez, C. Guadarrama-Perez, P.B. Balbuena, *J. Phys. Chem. A* 16 (2012) 1409–1416 <http://dx.doi.org/10.1021/jp208179e>.